

# In-situ synchrotron X-ray diffraction of hydroxyapatite-zirconia composite during conventional and flash sintering

I. Lavagnini, S. Ghose

To be published in "Journal of the European Ceramic Society"

January 2024

Photon Sciences

**Brookhaven National Laboratory**

**U.S. Department of Energy**

USDOE Office of Science (SC), Basic Energy Sciences (BES). Scientific User Facilities (SUF)

Notice: This manuscript has been authored by employees of Brookhaven Science Associates, LLC under Contract No. DE-SC0012704 with the U.S. Department of Energy. The publisher by accepting the manuscript for publication acknowledges that the United States Government retains a non-exclusive, paid-up, irrevocable, world-wide license to publish or reproduce the published form of this manuscript, or allow others to do so, for United States Government purposes.

## **DISCLAIMER**

This report was prepared as an account of work sponsored by an agency of the United States Government. Neither the United States Government nor any agency thereof, nor any of their employees, nor any of their contractors, subcontractors, or their employees, makes any warranty, express or implied, or assumes any legal liability or responsibility for the accuracy, completeness, or any third party's use or the results of such use of any information, apparatus, product, or process disclosed, or represents that its use would not infringe privately owned rights. Reference herein to any specific commercial product, process, or service by trade name, trademark, manufacturer, or otherwise, does not necessarily constitute or imply its endorsement, recommendation, or favoring by the United States Government or any agency thereof or its contractors or subcontractors. The views and opinions of authors expressed herein do not necessarily state or reflect those of the United States Government or any agency thereof.

# **In-situ synchrotron X-ray diffraction of hydroxyapatite-zirconia composite during conventional and flash sintering**

Isabela R. Lavagnini<sup>1,2,3</sup>; João V. Campos<sup>3,4</sup>; Lílian M. Jesus<sup>3,5</sup>; Anderson O. Lobo<sup>6</sup>; Sanjit K. Ghose<sup>7</sup>; Rishi Raj<sup>3</sup>; Eliria M. J. A. Pallone<sup>1,2</sup>

<sup>1</sup>Postgraduate Programme in Materials Science and Engineering, Faculty of Animal Science and Food Engineering (FZEA), University of Sao Paulo (USP), 225 Duque de Caxias Norte Ave., ZIP code 13635-900 – Pirassununga, SP, Brazil

<sup>2</sup>Department of Biosystem Engineering, Faculty of Animal Science and Food Engineering (FZEA), University of Sao Paulo (USP), 225 Duque de Caxias Norte Ave., ZIP code 13635-900 – Pirassununga, SP, Brazil

<sup>3</sup>Department of Mechanical Engineering, University of Colorado at Boulder (UCB), Boulder, CO 80309-0427, USA.

<sup>4</sup>Center for Research, Technology and Education in Vitreous Materials, Department of Materials Engineering, Federal University of São Carlos (UFSCar), ZIP code 13565-905 – São Carlos, SP, Brazil

<sup>5</sup>Group of Advanced Functional Materials (MAFA), Department of Physics, Federal University of São Carlos (UFSCar), ZIP code 13565-905 – São Carlos, SP, Brazil

<sup>6</sup>LIMAV-Interdisciplinary Laboratory for Advanced Materials, BioMatLab, Department of Materials Engineering, UFPI - Federal University of Piauí, 64049-550 Teresina, PI, Brazil

<sup>7</sup>National Synchrotron Light Source II, Brookhaven National Laboratory, Upton, NY, 11973, USA

## **Abstract**

We conducted in-situ X-ray diffraction to study the crystalline phase evolution in hydroxyapatite-zirconia composites during both conventional and flash sintering processes. Additionally, we examined the thermal history and microstructure of the composite under these sintering conditions. Despite both sintering methods reaching similar average temperatures, they yielded distinct results in terms of crystalline phase composition and microstructure. In the flash sintered samples, we observed a complete transformation of hydroxyapatite into  $\alpha$ -tricalcium phosphate and a complete tetragonal to cubic phase transition in zirconia. Conversely, the conventionally sintered samples remained practically stable. Notably, the flash sintered samples exhibited needle-like microstructures, which were absent in their conventionally sintered counterparts. This divergence suggests that the application of an electric field plays a role in generating athermal effects during the sintering of hydroxyapatite-zirconia composites.

**Keywords:** flash sintering; electric field; athermal effects; composites; biomaterials.

## Introduction

The hydroxyapatite-zirconia (HZ) composite shows significant potential for use in biomaterial applications due to the combination of the biological properties of hydroxyapatite [1–3] with the mechanical properties of zirconia [4–6]. As interest in the hydroxyapatite-zirconia composite continues to grow, adopting faster sintering techniques with lower furnace temperatures can potentially reduce production costs and improve the final product properties. Flash sintering (FS) [7] is a technique used to sinter ceramics in a remarkably short time by applying an electric field directly to the material. This process occurs at a lower furnace temperature compared to traditional sintering techniques, resulting in energy savings. Since its first report, FS has been applied in a wide range of materials [8–12], but its mechanisms are still under debate. It has been shown that FS is particularly efficient in the processing of composites [13], which are challenging to sinter using conventional heating methods. This is because each material within the composite can exhibit a different shrinkage rate, leading to a final product with low densification.

The use of in-situ characterization techniques provides a highly accurate way to evaluate the impact of specific parameters in materials processing and their final properties. In the case of FS, such experiments can also bring light into its mechanisms. In particular, in-situ X-ray diffraction (XRD) has growing attention because FS has been shown to affect the crystallization pathway of flash processed samples when compared to conventional sintering. For instance, in a pioneering study, Lebrun et al. [14] conducted in-situ XRD during FS of 3YSZ (3 mol% yttria stabilized zirconia). The experiments revealed that, after applying electric current for some time, a new crystalline phase emerged. The temperature of the 3YSZ samples was measured by the Pt-standard method and did not reach the zirconia phase transformation (tetragonal to cubic) temperature. The intensity of the diffraction peaks of the new phase, identified as the cubic zirconia, increased with time in the FS experiments. Furthermore, the authors observed that this phase gradually disappeared when the power supply was turned off, suggesting that during FS structural defects (such as oxygen vacancies) are formed and would be responsible for the emergence of the new phase. The authors then proposed that the energy of electric polarization played a crucial role in the nucleation and growth of the cubic structure.

Subsequently, several studies have used in-situ XRD either to tackle the behavior of crystalline phases of various materials during FS [15–20] or as a way to more accurately measure the real temperature of the sample during the flash event [21–23]. Using this approach, Campos et al. [21] showed that during FS the total conductivity of 3YSZ follows an Arrhenius-like behavior. In other words, the commonly reported non-linearity of materials conductivity during FS is likely related to the use of the furnace temperature (and not the real sample temperature) on the Arrhenius plots of conductivity.

Given this perspective, this work aimed at using in-situ X-ray diffraction to assess, for the first time, the effects of FS on the development of crystalline phases of the HZ composite when compared to conventional sintering. The thermal history and microstructure of the hydroxyapatite-zirconia composite under both sintering conditions are also analyzed.

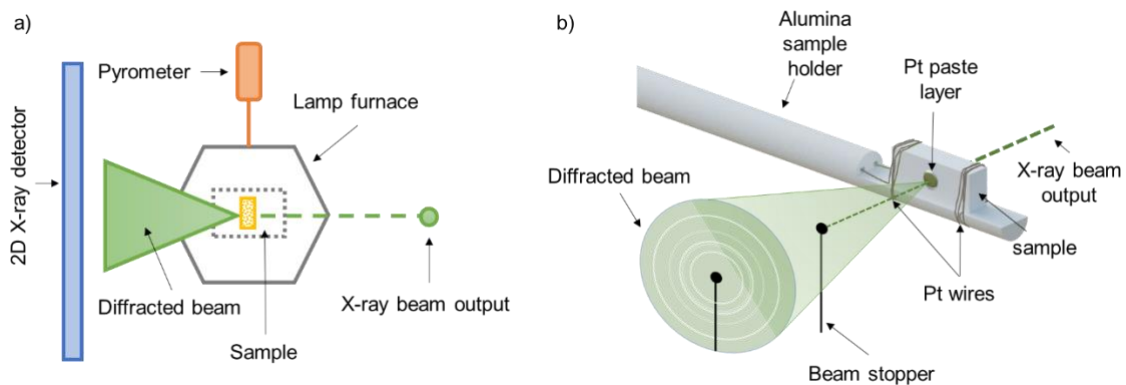
### **Experimental procedure**

To prepare the hydroxyapatite-zirconia composite, we used nanometric hydroxyapatite (HAp) powders synthesized through a wet chemical method [24] and commercial 3YSZ powders (TZ-3Y-E Tosoh). The powders were mixed with alcohol at a 1:1 weight ratio of HAp and 3YSZ. We added 0.5%wt. polyvinyl alcohol (PVA) binder solution to the suspension, and then subjected it to 8 hours of milling in a vibratory mill. After milling, the alcohol was completely removed in a muffle at 80 °C for 24 hours. Next, we uniaxially pressed the powder mixture into rectangular bars with a cross-sectional area of 1.5 x 3.5 mm and a length of 4.4 mm, applying a pressure of 280 MPa. Finally, the samples were calcined at 600 °C for 1 hour, with a heating rate of 10 °C per minute for removing the binder.

The in-situ XRD experiments were conducted at the National Synchrotron Light Source - II (NSLS-II) of the Brookhaven National Laboratory (BNL) in New York, at the XPD 28ID-2 beamline, with a wavelength of 0.1949 Å. The X-ray diffraction (XRD) patterns were measured using a large-area 2D PerkinElmer detector (2048 Å~ 2048 pixels, 200 Å~ 200 μm<sup>2</sup> each). A quadrupole lamp furnace [25] was employed to heat the samples during the experiments. Figure 1(a) illustrates the setup configuration. The furnace consisted of three openings: (1) an opening for the X-ray beam entrance; (2) an opening for the diffracted X-ray beam to exit; and (3) a top opening for

temperature measurement using a pyrometer. To align the beam with the sample and apply the electric field during furnace heating, an alumina sample holder was used. Platinum wires were employed to establish the connection between the power source and the sample. The wires worked as electrodes, with their ends wrapped around the rectangular samples. Platinum paste was applied to enhance the contact between the platinum wires and the sample. Figure 1(b) shows a schematic of the sample, the sample holder, and electrodes configuration.

Figure 1 (a) Illustration of the experimental setup configuration, (b) alumina sample holder and rectangular bar sample with platinum wires (electrodes) wrapped around its edges.



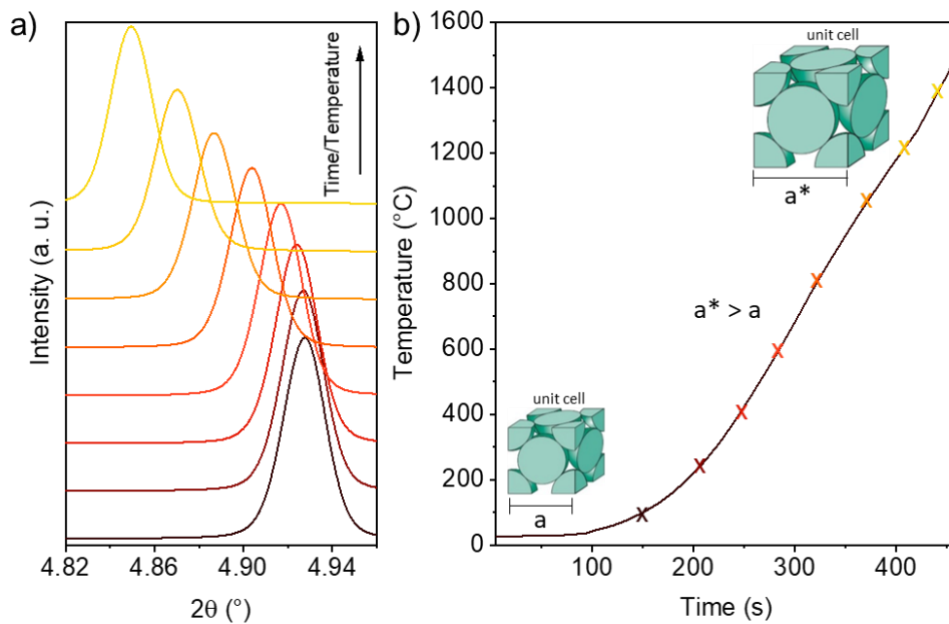
During FS, the DC electric field and electric current density were measured at a rate of 10 points per second, and a complete diffraction pattern was recorded every second. FS was performed isothermally, i.e., the power supply was activated only when the furnace reached 1000 °C (with a heating rate of 30 °C min<sup>-1</sup>). An electric field of 500 V cm<sup>-1</sup> was applied and a maximum electric current density of 20 mA mm<sup>-2</sup> was set. Once the pre-set current density was reached, the power supply remained on for 10 seconds (stage III of FS). Conventional sintering was carried out up to 1400 °C with a dwell time of 5 minutes and a heating rate of 30 °C min<sup>-1</sup>.

The in-situ XRD results obtained from these experiments were captured as images by the 2D detector. To create 1D diffraction patterns in the form of intensity versus diffraction angle ( $2\theta$ ), the captured images were integrated using the open-source software Dioptas [26]. Rietveld refinement was employed to determine and quantify the phases present in the diffraction patterns by GSAS-II software [27].

The samples temperatures were measured using the Pt-Standard method [23,28]. A thin layer of platinum paste was applied to the middle area of the larger surface of the rectangular sample. The positioning of the platinum paste layer allowed the X-ray beam to pass through it upon exiting the sample. The sample was heated

up to 1500 °C without applying an electric field and the changes in the peak position of the (1 1 1) plane of cubic platinum were measured for calibration. The shifts in the peak positions of platinum are related to the expansion of the material's unit cell volume due to heating. Therefore, it is possible to establish a correlation between the peak position ( $2\theta$ ) and the temperature using the platinum's thermal expansion equation [29]. Figure 2(a) illustrates the variation in the peak position of platinum in the (1 1 1) plane as the furnace temperature increases and Figure 2(b) shows the temperature calculated with Pt-standard for each peak position. It is evident that the peak shifts towards the left as the sample is heated.

Figure 2 (a) XRD pattern for the platinum peak in the (1 1 1) plane at different temperatures and (b) temperature calculated by the Pt-standard referring to the  $2\theta$  position of the platinum peak in the (1 1 1) plane during one of the experiments (more details on the experimental setup in Figure 1 (b)).



The sample position on the sample holder can affect the initial position of the peaks (a slight difference in  $2\theta$  value can be obtained for each sample). Thus, an XRD pattern was obtained before and after each experiment at room temperature to act as a reference for the initial and final positions of the platinum peaks.

The microstructure at the fractured surfaces of the samples was analyzed using scanning electron microscopy (SEM, FEG-XL 30; Philips). Energy-dispersive X-ray spectroscopy analysis (EDXS, Xplore 30; Oxford) with holding time of 300 s was carried out using spot-scan mode for comparative identification of elements dispersion in different areas of the samples' microstructure.

## Results and Discussion

To quantify the crystalline phases present in the starting powders, Rietveld refinement was conducted on an XRD pattern obtained from the green sample. The experimental and refined results, crystalline phases, and their respective percentages are presented in Figure 3. The refinement was successfully performed using the ICSD#86603 and the ICSD#26204 cards for 3YSZ (tetragonal) and HAp (hexagonal), respectively. The crystalline phases quantities in the green composite, obtained through the Rietveld refinement (which are included in Table 1) are in accordance with the experimental procedure employed, where production of a composite with 50% wt. of HAp and 50% wt. of 3YSZ was aimed. These green samples were then sintered either conventionally or via FS.

Figure 3 Result of the Rietveld refinement for the XRD pattern of the hydroxyapatite-zirconia composite before sintering.

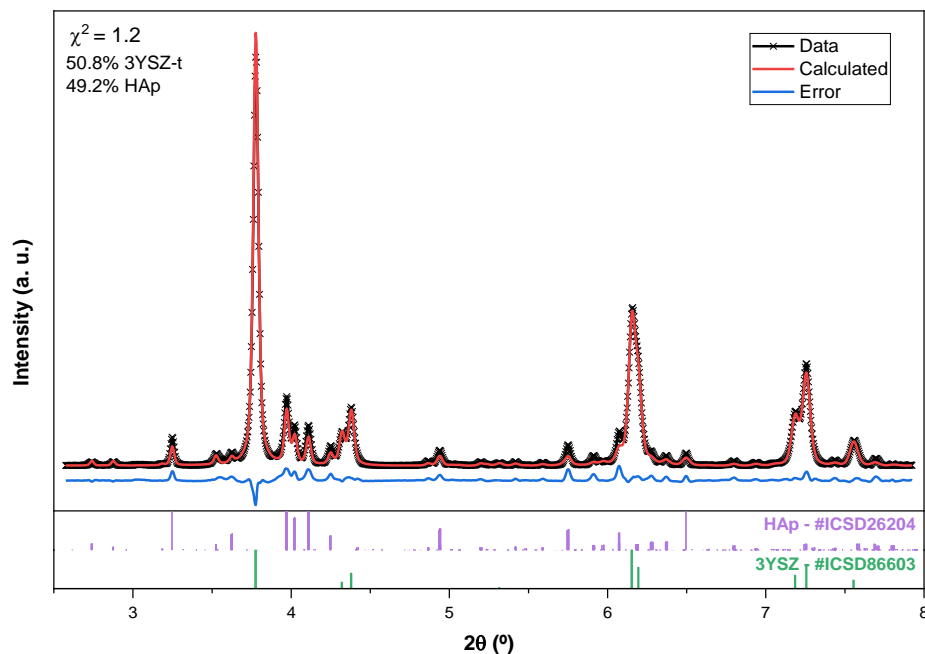
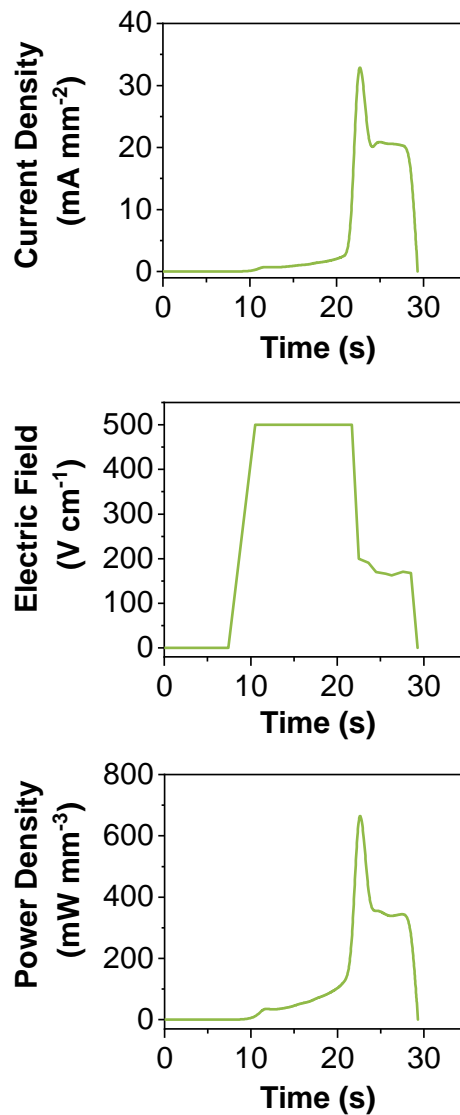


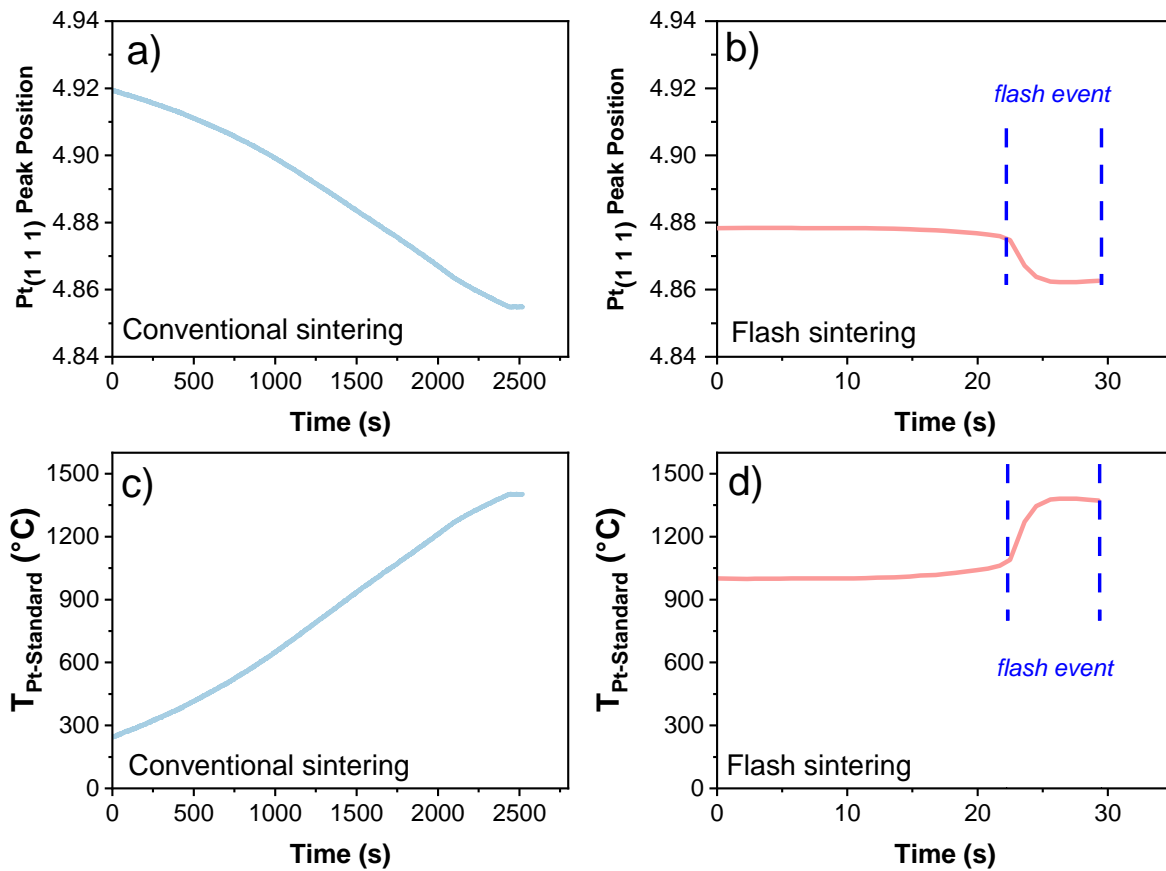
Figure 4 illustrates the time-dependent curves of current density, electric field, and power density during FS for the hydroxyapatite-zirconia composite. In this isothermal FS experiment, after applying a constant electric field of  $500 \text{ V cm}^{-1}$ , the electric current density began to rise and the flash event occurred after 12 s (*i.e.*, duration of Stage I of FS).

Figure 4 Curves of current density, electric field, and power density as a function of time for the flash sintered hydroxyapatite-zirconia composite.



The samples temperature during processing were monitored using the Pt-Standard method. Figure 5(a) display the shift of the peak in the (1 1 1) plane of cubic platinum during conventional sintering and Figure 5(b) during FS, while Figure 5(c) shows the curves of temperature calculated using this method for conventional sintering and Figure 5(d) for FS. In the case of conventional sintering, the Pt peak position gradually shifted as the sample temperature correspondingly increased, in accordance with the programmed heating rate. Conversely, during FS, the shift of the Pt peak position was abrupt rather than gradual, corresponding to an extremely rapid heating rate of  $\sim 10^4$  °C min<sup>-1</sup>. Furthermore, the Pt-Standard method allowed for an accurate estimation of the maximum temperature attained by the hydroxyapatite-zirconia composite during FS, which was approximately 1370 °C.

Figure 5 Peak position of the (1 1 1) plane of cubic platinum for (a) conventional sintering and (b) flash sintering; and temperature calculated by the Pt-Standard method for (c) conventional sintering and (d) flash sintering.



As in-situ XRD measurements were carried out during both sintering processes, a series of patterns were collected over time, enabling the examination of changes in the crystalline phases as a function of the composite's surface temperature. Starting with the conventionally sintered hydroxyapatite-zirconia composite, Figure 6 shows a 2D mapping of the XRD patterns to facilitate the observation of any structural change during the monitored time interval, which correlates proportionally with the temperature in this case. The patterns are displayed with respect to the collection time (y-axis) and the  $2\theta$  diffraction angle (x-axis). The intensity values are represented using colors. With increasing time, consequently, temperature, the HAp and 3YSZ peaks exhibit a shift towards the left, attributed to the thermal expansion of the materials' unit cells. Additionally, as the temperature rises, there is a noticeable enhancement in the intensity of all peaks, indicating grain/crystallite growth. Furthermore, it is possible to observe the emergence of new peaks at high temperatures ( $\sim 1300$  °C, which corresponds to  $\sim 38$  min on Figure 6), indicating the formation of secondary phases. Rietveld refinement was then performed

in a pattern collected at 1400 °C to evaluate these emerging phases, the results of which are presented in Table 1. The new peaks correspond to the crystalline phases of  $\alpha$ -TCP (ICSD#923) and  $\beta$ -TCP (ICSD#97500), suggesting a partial transformation of HAp crystalline structure during conventional heating.

Figure 6 Time resolved XRD patterns of the conventionally sintered hydroxyapatite-zirconia composite in a 2D view.

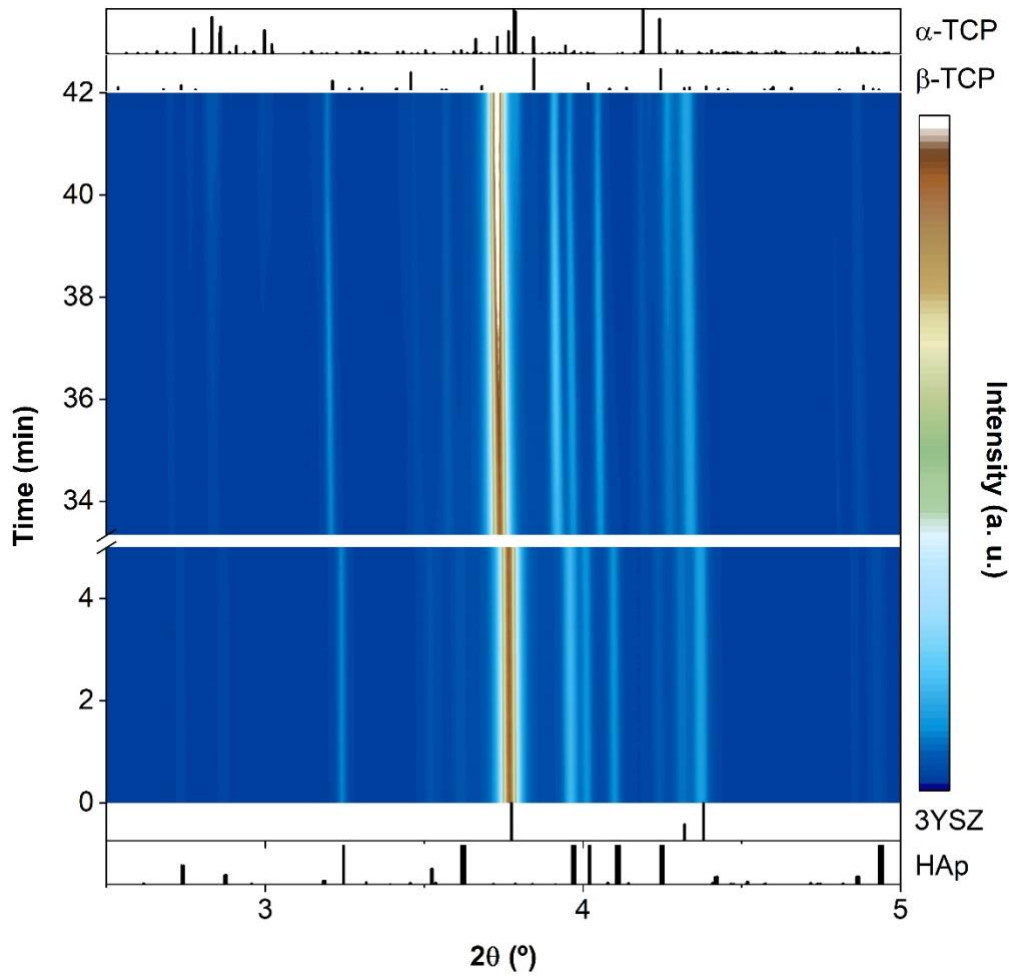
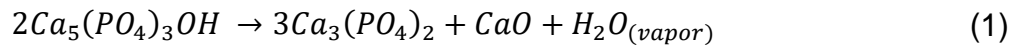


Table 1 Quantities of the crystalline phases calculated through Rietveld refinement in the patterns corresponding to the green sample, during conventional sintering at 1400 °C, after conventional sintering at room temperature, during flash sintering at 1370 °C and after flash sintering at room temperature for the hydroxyapatite-zirconia composite.

Temperature	Crystalline Phases (%)				
	3YSZ-t	Y/CaSZ-c	HAp	α-TCP	β-TCP
Green sample	50.8	-	49.2	-	-
CS - 1400 °C	54.6	-	36.4	8.3	0.7
CS - Room temperature after firing	52.8	-	38.8	6.9	1.5
FS - 1370 °C	-	72.3	-	27.7	-
FS - Room temperature after firing	-	63.1	-	33.9	3.0

Nilen and Richter [30] demonstrated that around 1300 °C, HAp undergoes dehydroxylation and partially transforms into β-TCP ( $Ca_3(PO_4)_2$ ), according to Equation 1:



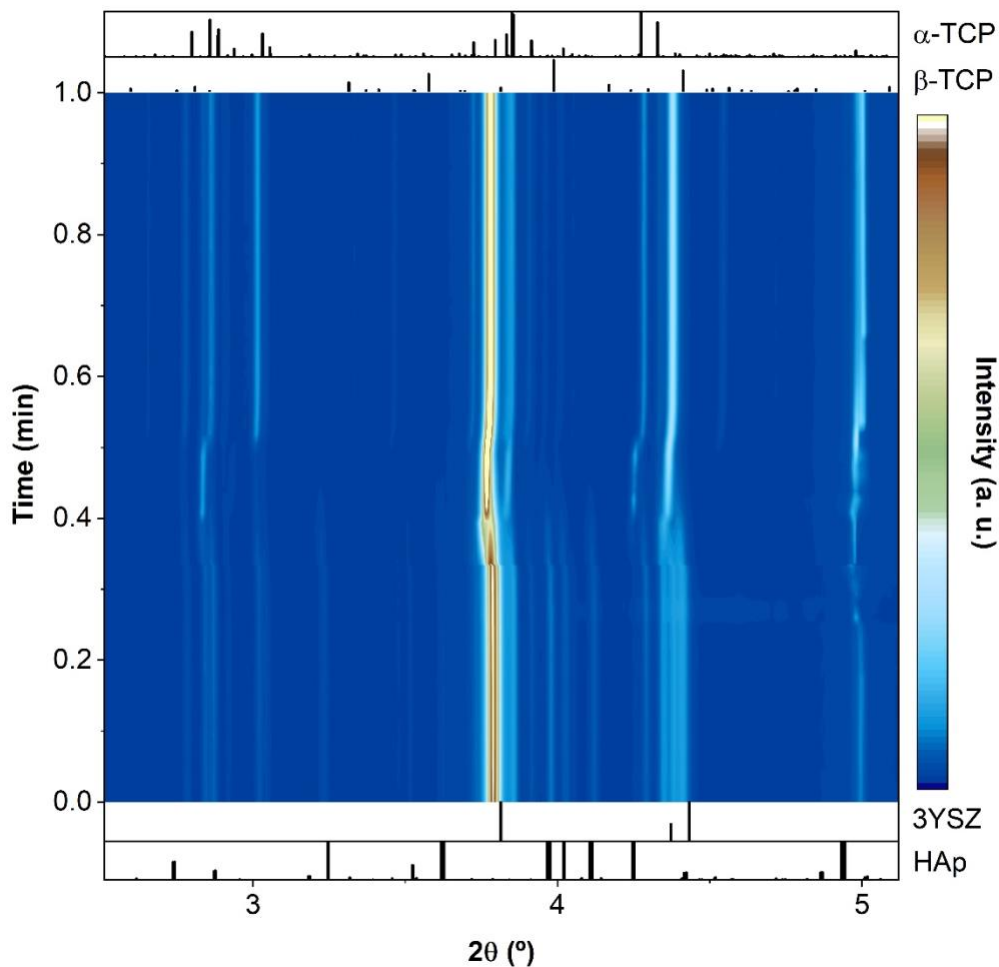
In the refinement results (Table 1), a higher amount of the α-TCP is observed compared to the β-TCP phase, likely because as the temperature continues to increase, the β-TCP phase (rhombohedral) partially transforms into the α-TCP phase (monoclinic) [31,32].

Regarding the 3YSZ, it is observed that both during (1400 °C) and after conventional heating, it remains tetragonal, without the presence of monoclinic or cubic structures. Nonetheless, the 3YSZ fraction in the composite increased during heating, compared to the initial value (green sample), and decreased again after the end of sintering. This change may be related to the variation in the amount of HAp within the composite due to the loss of water from its structure and simultaneous partial conversion in CaO (as shown in Equation 1).

The XRD patterns of the HZ composite collected during the in-situ FS experiments are presented in Figure 7 in a 2D view. In this case, the progression of time can also be correlated with the temperature increase but not in a linear way. Thus, it is possible to observe the consequences in peak position due to the high heating rate, which in this case is provided by the Joule effect. One can notice the moment when the flash event is initiated, indicated by a steep left shift of the diffraction peaks. This behavior can be clearly observed by looking at the most intense peak

corresponding to the (1 1 1) plane of 3YSZ at  $2\theta = 3.74^\circ$ , occurring around 0.4 min. These shifts are result of the rapid heating of the material when the electric current passing through it increases abruptly. Furthermore, peaks corresponding to various planes of HAp quickly disappear after the initiation of the electric current passage through the composite while peaks from the crystalline planes (1 1 0) and (0 0 2) of 3YSZ (at  $2\theta = \sim 4.3^\circ$ ) convert into a single peak during the flash event, indicating a phase transformation.

Figure 7 Time resolved XRD patterns of the flash sintered hydroxyapatite-zirconia composite in a 2D view.



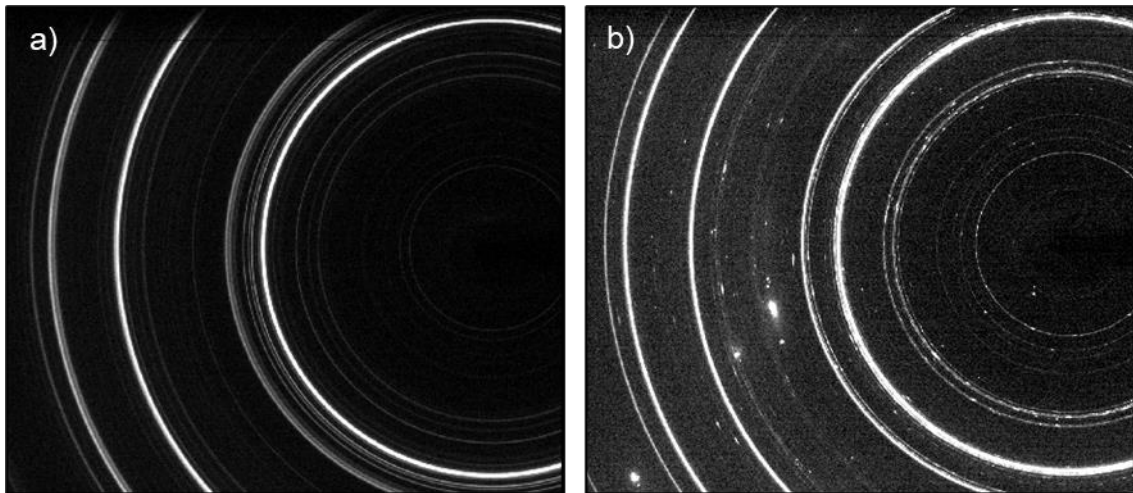
Once again, Rietveld refinement was conducted to quantify the phases present at the end of the flash experiment ( $\sim 1370^\circ\text{C}$ ) as well as at room temperature after FS, the results of which are included in Table 1. These findings revealed that HAp underwent the same crystalline phase conversion to  $\alpha$ -TCP and  $\beta$ -TCP as observed in the conventional sintering experiment. However, during FS, the decomposition was significant, leading to a total conversion into  $\alpha$ -TCP at the end of the FS experiment.

It is noteworthy that, even at room temperature after firing, the presence of  $\beta$ -TCP was minimal. It is known that the high-temperature  $\beta \rightarrow \alpha$  transformation is typically reversible during the cooling process, but this transformation can be hindered when thermal quenching is employed [33–36]. In FS, the  $\alpha \rightarrow \beta$  conversion during cooling was inhibited due to the natural quenching effect that occurs when the electric field is turned off, as previously verified [37]. During the slow cooling of conventional sintering, the  $\alpha \rightarrow \beta$  transformation typically occurs [37]. In this study, the  $\alpha \rightarrow \beta$  conversion was also inhibited for conventional sintering (Table 1) due to the experimental setup with an open lamp furnace, meaning that turning it off resulted in air quenching.

Besides HAp full decomposition at the end and after the FS experiment, one can observe in Table 1 that, different from the conventional sintering experiment, all the 3YSZ was converted to a cubic structure. As reported previously [14,21], this transformation from tetragonal to cubic phase could be attributed to the high temperature reached. Nevertheless, in those studies, the cubic phase did not persist upon cooling. In contrast, in the present case, the cubic phase was observed even at room temperature after FS. Additionally, in the conventional sintering the sample reached a similar temperature and no cubic 3YSZ was observed. Thus, one plausible explanation for this phenomenon is the incorporation of  $\text{Ca}^{2+}$  ions into the 3YSZ structure, serving as co-dopants. This doping would account for the emergence of the cubic phase and its stabilization. This hypothesis also explains the absence of patterns related to CaO, as it is a product of HAp decomposition into  $\beta$ -TCP, as depicted in Equation 1. For these refinements, the 8YSZ card (ICSD#195189) was used, with the addition of  $\text{Ca}^{2+}$  as a dopant partially substituting  $\text{Zr}^{4+}$  ions within the structure. The optimal result showed a fraction of 2%  $\text{Y}^{3+}$  and 7%  $\text{Ca}^{2+}$ , abbreviated as Y/CaSZ.

Figure 8 depicts the Debye-Scherrer arcs of the diffracted planes from the samples at the high temperature conditions during: (a) conventional sintering (1400 °C) and (b) FS (1370 °C). It is evident that the arcs associated with the composite during conventional sintering appear as continuous lines, whereas in FS, not all observed arcs are continuous. In FS, the arcs marked by 'dotted' lines correspond to the planes of the  $\alpha$ -TCP crystalline phase, while the continuous lines represent Y/CaSZ (yttria and calcium stabilized zirconia). According to He [38] and Bramble et al. [39], the presence of these 'dotted' lines indicates preferential grain growth in the respective planes (texturing).

Figure 8 Debye-Scherrer arcs of the diffracted hydroxyapatite-zirconia composite captured by the 2D detector for (a) conventional sintering at 1400 °C and (b) flash sintering at 1370 °C.



Indeed, in the ICSD#923 card, standard for the  $\alpha$ -TCP crystalline phase, the intensity ratio between the diffracted peaks corresponding to the (3 3 -2) and (2 6 -4) planes ( $I_{(3\ 3\ -2)}/I_{(2\ 6\ -4)}$ ) is found to be 0.32. However, in the diffractogram collected at high temperature during FS, these peaks exhibit a ratio  $I_{(3\ 3\ -2)}/I_{(2\ 6\ -4)}$  of 0.78. This discrepancy in the peaks ratio of the  $\alpha$ -TCP phase alongside the dotted lines present in Figure 8(b) indicate that during FS this phase exhibit texture, suggesting directional grain growth.

To further investigate texturization effects, we performed SEM analysis. Figure 9 showcases micrographs of hydroxyapatite-zirconia composite conventionally and flash sintered. The microstructure of the composite produced by FS confirms the hypothesis drawn from the Debye-Scherrer arcs in Figure 8. It reveals a microstructure comprising micrometer-sized needles, with some arranged in a dandelion-like flower shape. In contrast, the conventionally sintered samples do not exhibit similar microstructures. As shown in Figure 10, these micro-needles are generally present across the analyzed fractured surface. In Figure 10(b) it is possible to see the interface between sphere-like and needle-like grains, while Figure 10(c) and (d) focus on each type of grain. Taking a closer look at the spherical grains in Figure 10 (c), one can notice that an amorphous-like phase surrounds them.

Figure 9 Micrographs of fractured surface of hydroxyapatite-zirconia composite (a) conventionally and (b) flash sintered.

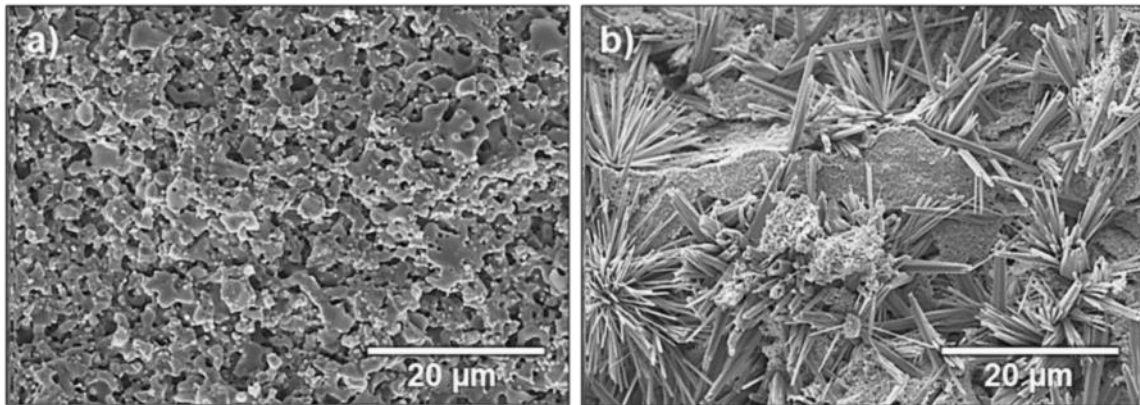
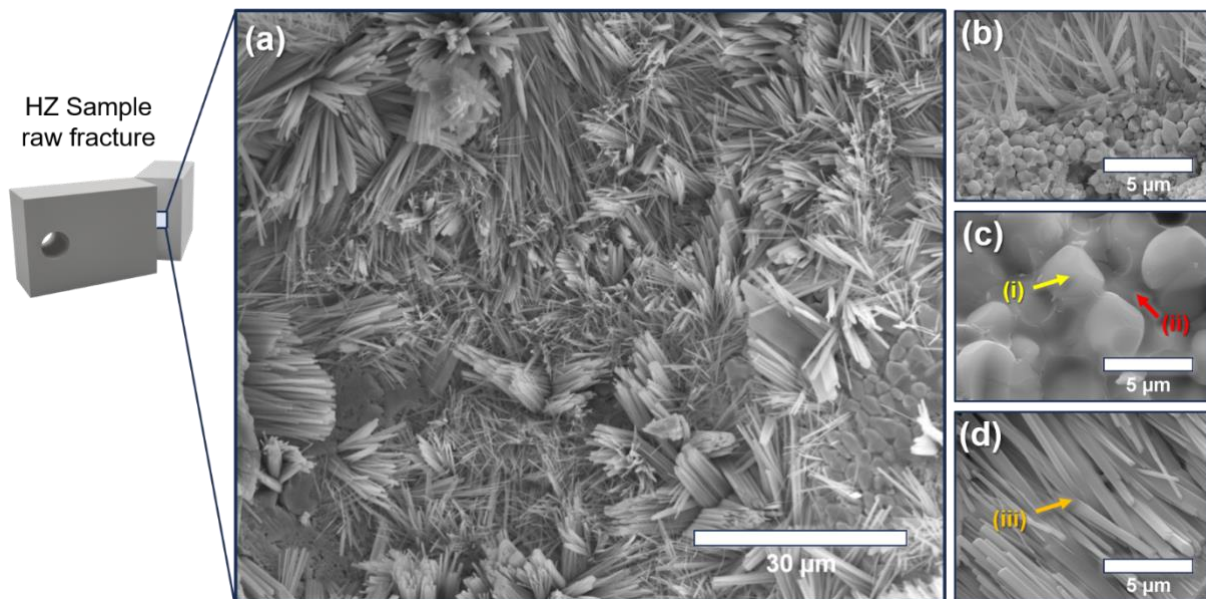


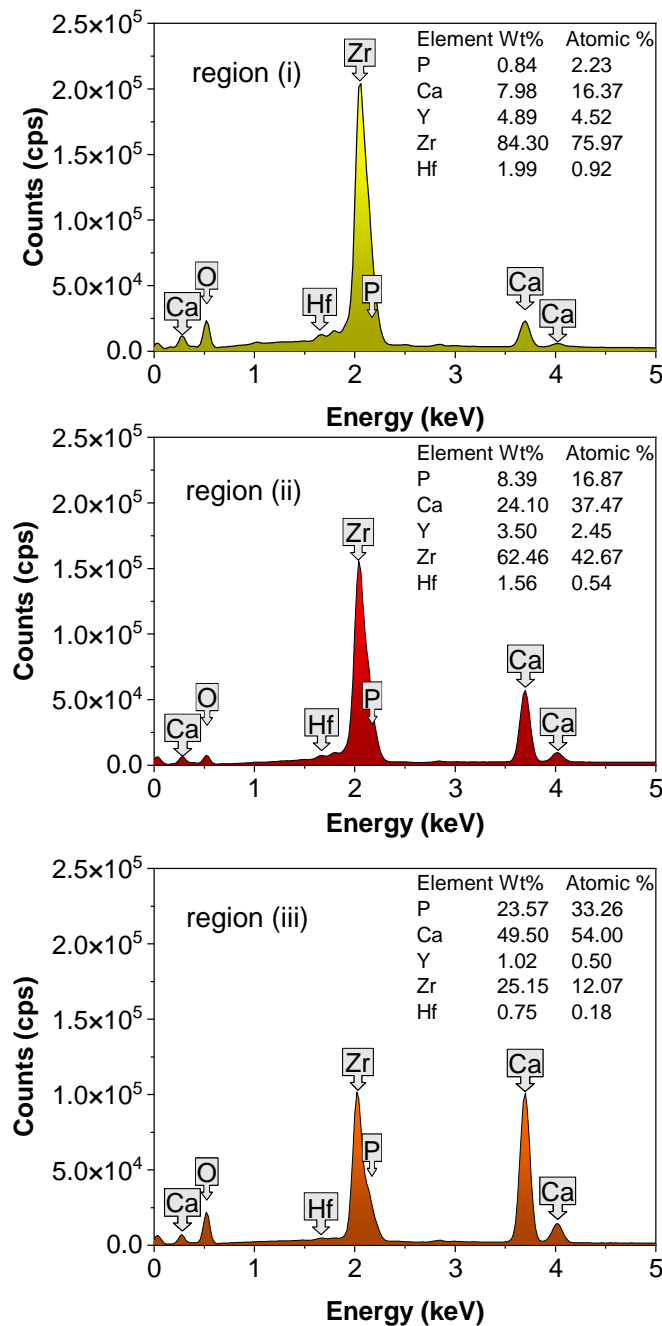
Figure 10 (a) Micrographs depicting the fractured surface of a flash-sintered hydroxyapatite-zirconia composite, emphasizing the distribution of needle-like structures within the sample. Insets (b), (c), and (d) illustrate distinct regions: (b) interfaces between spherical grains and needle-like structures, (c) amorphous grain boundaries within spherical grains, and (d) needle-like structures. Arrows (i), (ii), and (iii) indicate locations where spot-scan Energy Dispersive X-ray (EDX) analysis was performed to assess chemical composition (refer to Figure 11 for detailed information).



Spot-scan mode EDXS analysis was performed at the three different regions highlighted in Figure 10(c) and (d): (i) on a spherical grain, (ii) on an amorphous-like grain boundary, and (iii) on a needle-like structure. The results are depicted in Figure 11. The quantification highlights that the concentration of Ca and P is higher in region (ii) and (iii) when compared with region (i). This analysis, associated with the presence of 'dotted' lines corresponding to the planes of the  $\alpha$ -TCP crystalline phase in the Debye-Scherrer arcs in Figure 8 (suggesting texturing of that phase) and with the temperature melting point of both materials (3YSZ  $\sim$ 2700 °C [40] and HAp  $\sim$ 1600 °C

[41]), suggests that the crystalline structure of the micro-needles is predominantly  $\alpha$ -TCP. It's noteworthy that the energy associated with the P K $\alpha$  decay (2.013 keV) closely matches the Zr L $\alpha$  energy (2.042 keV), making it challenging to differentiate these two elements by EDXS. However, as Hf is a common impurity in 3YSZ powder (up to 5 wt.% according to the vendor) but not present in HAp, its near-zero content in the needle-like area (iii) indirectly confirms that the needle structures primarily comprise calcium phosphates. Notably, the presence of calcium in region (i), where phosphorous content was negligible, supports our claim that calcium co-doped the zirconia and stabilized it in its cubic phase.

Figure 11 Results of spot-scan mode EDXS analysis for three different regions highlighted in Figure 10: (a) on a spherical grain (i), (b) on an amorphous-like grain boundary (ii), and (c) on a needle-like structure (iii).



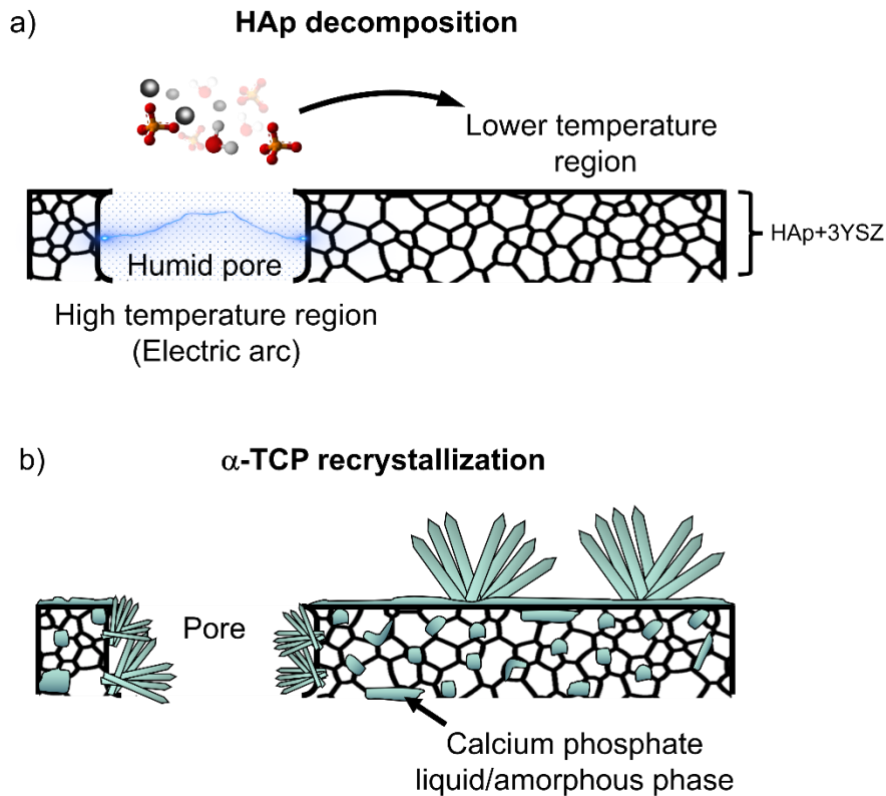
Previous reports have documented the presence of needle-like microstructures in flash sintered ZnO samples [42,43]. Zhang, Jung, and Luo [43] observed micro-needles with lengths ranging from approximately 5 to 30  $\mu\text{m}$ , whereas Phuah et al. [42] observed nanoscale-sized needles (<100 nm). Both studies employed a continuous electric field and noted its influence on the alignment of these microstructures, with most needles growing towards the anode. Additionally, the authors reported that these microstructures were often found in proximity to hotspot

regions. Consequently, they propose that the formation of these needles may be attributed to local melting and the generation of a liquid or even gaseous phase within their material.

Phuah et al. [42] discuss that the formation of nano and micrometer-sized needles is likely attributed to the vapor-liquid-solid (VLS) mechanism. The VLS mechanism involves the generation of liquid droplets and gas compounds within the material, followed by reoxidation and crystallization. The growth of these microstructures through the VLS mechanism necessitates the presence of gaseous precursors. Consequently, the emergence of gas compounds within the material is only possible at extremely high local temperatures. Worth noting here that Pt-standard represents the average temperature of the sample.

Here, we suggest a VLS mechanism to explain the nucleation and growth of the micro-needles in the hydroxyapatite-zirconia composites, the schematic of which is presented in Figure 12. It is hypothesized that most of the applied electric current initially conducts through the 3YSZ phase (which is more conducting), creating a percolation path and elevating the local temperature near these paths, as it has been previously discussed for other composites [44]. Subsequently, the HAp phase reaches its decomposition temperature, releasing water vapor (as per Equation 1) and creating a humid atmosphere in the porous region of the green sample. The combination of a high local electric field, ionic conduction characteristics of HAp [37] and the humid environment results in local arcing, leading to local melting and even vaporization of the calcium phosphate constituents. These compounds are then reincorporated and recrystallized in the pore's walls and in neighboring regions when the arcing ceases. The simultaneous application of an electric field during the reincorporation promotes a preferential growth direction, leading to the formation of the observed micro-needles, as is seen in hydrothermal microwave-assisted process [45–47]. It is worth noting that alternative mechanisms, such as electromigration, might also play a role in the formation of these micro-needles [48,49].

Figure 12 Illustration of the Vapor-Liquid-Solid mechanism operating in the hydroxyapatite-zirconia composite during flash sintering and subsequent recrystallization of the material.



In summary, FS successfully transformed HAp into the  $\alpha$ -TCP phase and tetragonal zirconia into its cubic structure. In contrast, conventional sintering retained zirconia in its initial tetragonal phase, with only a slight conversion of HAp into  $\alpha$ - and  $\beta$ -TCP. Although the Pt-standard indicated similar maximum temperatures for both methods (1400 - 1370 °C), it is crucial to note that flash-sintered samples can exhibit significant thermal gradients throughout the material during the flash event. Extensive exploration through finite element models [50,51] and grain size assessments across various regions within a single sample [52,53] has revealed this phenomenon.

Furthermore, the temperature estimate provided by the Pt-standard primarily reflects the surface temperature of the sample, potentially differing from the core temperature. Consequently, the temperature measured by the Pt-standard method represents a lower bound for the average temperature achieved by the sample. Localized hotspots may have emerged in different regions, leading to local thermal gradients.

The presented findings, including evidence of melting in Figure 10 and the phase transformation from HAp to  $\alpha$ -TCP, strongly suggest that the sample's interior

experienced significantly higher temperatures than those recorded by the Pt-standard method. In cases of local overheating, elements with high partial pressure are expected to vaporize, influencing the sample's final composition, and altering the crystalline phases present. This observed phenomenon supports the potential occurrence of the VLS mechanism. According to Chaim [54,55], one of the proposed mechanisms for FS involves a high concentration of electric current inducing localized overheating at particle-particle contacts, leading to the formation of a liquid phase in that specific region. The presence of this liquid phase facilitates the diffusion process, explaining the observed rapid densification in FS [54,55], which aligns with the formation of needles within a remarkably short duration of 10 seconds.

The electric field applied during FS may also be playing a role, generating athermal effects on the hydroxyapatite-zirconia composite, which facilitated these different outcomes. The electric field might be inducing an increase in the number of oxygen vacancies in the 3YSZ structure. This phenomenon is supported by the observation of the blackening effect [56,57] and the formation of cavitation pores [52,58]. Consequently, it is proposed that the higher concentration of oxygen vacancies facilitates the doping of  $\text{Ca}^{2+}$  ions into the 3YSZ structure. Considering the proposed VLS process for HAp, the application of an electric field may influence the preferential growth of specific crystal planes during the recrystallization of the molten phase which explains the observed texturing. Such an effect can also be characterized as athermal (related to the electric field and not to temperature). Nevertheless, it is important to emphasize that there is a difference in the heating rate between the experiments ( $30\text{ }^{\circ}\text{C min}^{-1}$  for conventional sintering and  $10^4\text{ }^{\circ}\text{C min}^{-1}$  for FS after the flash event), which may also play a significant role in the attainment of these distinct results.

Finally, the observation of microneedles draws attention to the capacity of FS to rapidly produce specific microstructures without the need for any type of additives (catalysts, seeds, single crystals, substrates, or precursors). Additionally, this needle-like structure exhibits special surface characteristics and has a high surface area. Thus, this morphology could potentially unveil new applications for this material, as showed by Wu et al. (2020) [59].

## Conclusion

The application of electric field and electric current during sintering of the hydroxyapatite-zirconia composite has a significant impact on the structural and microstructural evolution of the material. In conventional sintering, the resulting phases consisted mainly of tetragonal zirconia and hydroxyapatite, with small amounts of  $\alpha$ -tricalcium phosphate and  $\beta$ -tricalcium phosphate phases. On the other hand, in flash sintering the hydroxyapatite in the composite was fully converted to  $\alpha$ -tricalcium phosphate, and the zirconia was stabilized in its cubic phase (both during the flash and after cooling) due to the incorporation of  $\text{Ca}^{2+}$  ions into its structure. Furthermore, texturization effects were only verified in the flash sintering processed samples, where needle-like microstructures were formed. The results suggest that these differences are due to local overheating in some regions of the sample, which might have triggered a vapor-liquid-solid mechanism in flash-sintered samples. Despite the high local temperature reached by the flash-sintered samples, the application of an electric field plays a crucial role in generating athermal effects during the sintering of the hydroxyapatite-zirconia composite. However, it is important to note that the high heating rate during flash sintering should not be overlooked and might contribute as well to the distinct results obtained for FS compared to conventional sintering. Finally, the rapid processing obtained by flash sintering, coupled with the potential for lowering furnace temperatures, represents a significant advantage of this technique, allowing to produce this material with reduced energy consumption.

## Acknowledgements

National Council for Scientific and Technological Development (CNPq) [200573/2018-7, 150523/2022-0, 403978/2021-1, 310883/2020-2, and 404683/2018-5]. Coordenação de Aperfeiçoamento de Pessoal de Nível Superior - Brasil (CAPES) - Finance Code 001. São Paulo Research Foundation (FAPESP) [2019/03786-1, 2021/06509-9, 2019/14677-9, 2022/10604-0]. Office of Science of the Department of Energy, Grant/Award Number: DE-AC02 98CH10886. This research used 28ID-2 (XPD) beamline of the National Synchrotron Light Source II; a U.S. Department of Energy (DOE) Office of Science User Facility operated for the DOE Office of Science by Brookhaven National Laboratory under Contract No. DE-SC0012704. The authors

thank the Laboratory of Structural Characterization (LCE/DEMa/UFSCar) for the general facilities.

## References

- [1] A. Das, D. Pamu, A comprehensive review on electrical properties of hydroxyapatite based ceramic composites, *Mater. Sci. Eng. C*. 101 (2019) 539–563. <https://doi.org/10.1016/j.msec.2019.03.077>.
- [2] L. Schröter, F. Kaiser, S. Stein, U. Gbureck, A. Ignatius, Biological and mechanical performance and degradation characteristics of calcium phosphate cements in large animals and humans, *Acta Biomater.* 117 (2020) 1–20. <https://doi.org/10.1016/j.actbio.2020.09.031>.
- [3] S. Ferraris, S. Yamaguchi, N. Barbani, M. Cazzola, C. Cristallini, M. Miola, E. Vernè, S. Spriano, Bioactive materials: In vitro investigation of different mechanisms of hydroxyapatite precipitation, *Acta Biomater.* 102 (2020) 468–480. <https://doi.org/10.1016/j.actbio.2019.11.024>.
- [4] M. Dehestani, L. Ilver, E. Adolfsson, Enhancing the bioactivity of zirconia and zirconia composites by surface modification, *J. Biomed. Mater. Res. - Part B Appl. Biomater.* 100 B (2012) 832–840. <https://doi.org/10.1002/jbm.b.32647>.
- [5] J. Brzezińska-Miecznik, K. Haberko, M. Sitarz, M.M. Bućko, B. MacHerzyńska, R. Lach, Natural and synthetic hydroxyapatite/zirconia composites: A comparative study, *Ceram. Int.* 42 (2016) 11126–11135. <https://doi.org/10.1016/j.ceramint.2016.04.019>.
- [6] D. Singh, M. de la Cinta Lorenzo-Martin, F. Gutiérrez-Mora, J.L. Routbort, E.D. Case, Self-joining of zirconia/hydroxyapatite composites using plastic deformation process, *Acta Biomater.* 2 (2006) 669–675. <https://doi.org/10.1016/j.actbio.2006.06.004>.
- [7] M. Cologna, B. Rashkova, R. Raj, Flash sintering of nanograin zirconia in <5 s at 850°C, *J. Am. Ceram. Soc.* 93 (2010) 3556–3559. <https://doi.org/10.1111/j.1551-2916.2010.04089.x>.
- [8] C. Manière, G. Lee, E.A. Olevsky, Flash sintering of complex shapes, *Appl. Mater. Today*. 26 (2022) 101293. <https://doi.org/10.1016/j.apmt.2021.101293>.
- [9] K.S. Naik, P.P. Satardekar, J.A. Downs, V.M. Sglavo, Understanding the flash sintering behavior for hydroxyapatite, *J. Mater. Res.* 37 (2022) 1030–1036.

- <https://doi.org/10.1557/s43578-022-00521-5>.
- [10] J. V. Campos, I.R. Lavagnini, V.M. Zallocco, E.B. Ferreira, E.M.J.A. Pallone, A.C.M. Rodrigues, Flash sintering with concurrent crystallization of  $\text{Li}_{1.5}\text{Al}_{0.5}\text{Ge}_{1.5}(\text{PO}_4)_3$  glass, *Acta Mater.* 244 (2023) 118593. <https://doi.org/10.1016/j.actamat.2022.118593>.
- [11] F. Sun, P. Ji, L. Tan, J. Yang, Q. Tian, Q. Li, S. Lv, X. Su, Formation of eutectic microstructure in  $\text{Al}_2\text{O}_3\text{-GdAlO}_3\text{-ZrO}_2$  ceramics by flash sintering, *Ceram. Int.* 48 (2022) 16455–16460. <https://doi.org/10.1016/j.ceramint.2022.03.189>.
- [12] F.R. Monteiro, A.G. Storion, K. Ramos, L.M. Jesus, D. Pérez-Coll, G.C. Mather, A.L. Chinelatto, E.M. de J.A. Pallone, Influence of particle contact on flash sintering of ZnO and 8YSZ: Microstructure and electrical conductivity, *Ceram. Int.* 49 (2023) 36659–36668. <https://doi.org/10.1016/j.ceramint.2023.08.349>.
- [13] S.K. Jha, R. Raj, Electric Fields Obviate Constrained Sintering, *J. Am. Ceram. Soc.* 97 (2014) 3103–3109. <https://doi.org/10.1111/jace.13136>.
- [14] J.M. Lebrun, T.G. Morrissey, J.S.C. Francis, K.C. Seymour, W.M. Kriven, R. Raj, Emergence and Extinction of a New Phase during On-Off Experiments Related to Flash Sintering of 3YSZ, *J. Am. Ceram. Soc.* 98 (2015) 1493–1497. <https://doi.org/10.1111/jace.13476>.
- [15] H. Charalambous, S.K. Jha, J.S. Okasinski, T. Tsakalagos, Generation of electric-field stabilized zirconium monoxide secondary phase within cubic zirconia, *Scr. Mater.* 190 (2021) 22–26. <https://doi.org/10.1016/j.scriptamat.2020.08.026>.
- [16] B. Yoon, V. Avila, R. Raj, L.M. Jesus, Reactive flash sintering of the entropy-stabilized oxide  $\text{Mg}_{0.2}\text{Ni}_{0.2}\text{Co}_{0.2}\text{Cu}_{0.2}\text{Zn}_{0.2}\text{O}$ , *Scr. Mater.* 181 (2020) 48–52. <https://doi.org/10.1016/j.scriptamat.2020.02.006>.
- [17] V. Avila, B. Yoon, R.R. Ingraci Neto, R.S. Silva, S. Ghose, R. Raj, L.M. Jesus, Reactive flash sintering of the complex oxide  $\text{Li}_{0.5}\text{La}_{0.5}\text{TiO}_3$  starting from an amorphous precursor powder, *Scr. Mater.* 176 (2020) 78–82. <https://doi.org/10.1016/j.scriptamat.2019.09.037>.
- [18] S.K. Jha, J.M. Lebrun, K.C. Seymour, W.M. Kriven, R. Raj, Electric field induced texture in titania during experiments related to flash sintering, *J. Eur. Ceram. Soc.* 36 (2016) 257–261. <https://doi.org/10.1016/j.jeurceramsoc.2015.09.002>.
- [19] V. Avila, B. Yoon, S. Ghose, R. Raj, L.M. Jesus, Phase evolution during reactive flash sintering of  $\text{Li}_{6.25}\text{Al}_{0.25}\text{La}_3\text{Zr}_2\text{O}_{12}$  starting from a chemically prepared

- powder, *J. Eur. Ceram. Soc.* 41 (2021) 4552–4557. <https://doi.org/10.1016/j.jeurceramsoc.2021.02.054>.
- [20] B. Yoon, J. V. Campos, I.R. Lavagnini, V. Avila, J.M. Gardner, S.K. Ghose, L.M. Jesus, Phase evolution during conventional and reactive flash sintering of (Mg,Ni,Co,Cu,Zn)O via in situ X-ray diffraction, *J. Am. Ceram. Soc.* (2023) 1–12. <https://doi.org/10.1111/jace.19503>.
- [21] J. V. Campos, I.R. Lavagnini, V. Avila, B. Yoon, S. Ghose, R. Raj, E.M.J.A. Pallone, L.M. Jesus, On the Arrhenius-like behavior of conductivity during flash sintering of 3 mol% yttria stabilized zirconia ceramics, *Scr. Mater.* 203 (2021) 114093. <https://doi.org/10.1016/j.scriptamat.2021.114093>.
- [22] H. Charalambous, S.K. Jha, R.T. Lay, A. Cabales, J. Okasinski, T. Tsakalakos, Investigation of temperature approximation methods during flash sintering of ZnO, *Ceram. Int.* 44 (2018) 6162–6169. <https://doi.org/10.1016/j.ceramint.2017.12.250>.
- [23] K. Terauds, J.M. Lebrun, H.H. Lee, T.Y. Jeon, S.H. Lee, J.H. Je, R. Raj, Electroluminescence and the measurement of temperature during Stage III of flash sintering experiments, *J. Eur. Ceram. Soc.* 35 (2015) 3195–3199. <https://doi.org/10.1016/j.jeurceramsoc.2015.03.040>.
- [24] M.C. Barbosa, N.R. Messmer, T.R. Brazil, F.R. Marciano, A.O. Lobo, The effect of ultrasonic irradiation on the crystallinity of nano-hydroxyapatite produced via the wet chemical method, *Mater. Sci. Eng. C.* 33 (2013) 2620–2625. <https://doi.org/10.1016/j.msec.2013.02.027>.
- [25] P. Sarin, W. Yoon, K. Jurkschat, P. Zschack, W.M. Kriven, Quadrupole lamp furnace for high temperature (up to 2050K) synchrotron powder x-ray diffraction studies in air in reflection geometry, *Rev. Sci. Instrum.* 77 (2006) 093906. <https://doi.org/10.1063/1.2349600>.
- [26] C. Prescher, V.B. Prakapenka, DIOPTAS: a program for reduction of two-dimensional X-ray diffraction data and data exploration, *High Press. Res.* 35 (2015) 223–230. <https://doi.org/10.1080/08957959.2015.1059835>.
- [27] B.H. Toby, R.B. Von Dreele, GSAS-II: the genesis of a modern open-source all purpose crystallography software package, *J. Appl. Crystallogr.* 46 (2013) 544–549. <https://doi.org/10.1107/S0021889813003531>.
- [28] B. Yoon, D. Yadav, S. Ghose, P. Sarin, R. Raj, On the synchronicity of flash sintering and phase transformation, *J. Am. Ceram. Soc.* 102 (2019) 3110–3116.

- <https://doi.org/10.1111/jace.16335>.
- [29] T.A. HAHN, R.K. KIRBY, Thermal expansion of platinum from 293 to 1900K, AIP Conf. Proc. 87 (1972) 87–95. <https://doi.org/10.1063/1.2948578>.
- [30] R.W.N. Nilen, P.W. Richter, The thermal stability of hydroxyapatite in biphasic calcium phosphate ceramics, J. Mater. Sci. Mater. Med. 19 (2008) 1693–1702. <https://doi.org/10.1007/s10856-007-3252-x>.
- [31] R.A. Youness, M.A. Taha, M.A. Ibrahim, In vitro bioactivity , molecular structure and mechanical properties of zirconia-carbonated hydroxyapatite nanobiocomposites sintered at different temperatures, Mater. Chem. Phys. 239 (2020) 122011. <https://doi.org/10.1016/j.matchemphys.2019.122011>.
- [32] M. Yashima, A. Sakai, T. Kamiyama, A. Hoshikawa, Crystal structure analysis of b-tricalcium phosphate  $\text{Ca}_3(\text{PO}_4)_2$  by neutron powder diffraction, J. Solid State Chem. 175 (2003) 272–277. [https://doi.org/10.1016/S0022-4596\(03\)00279-2](https://doi.org/10.1016/S0022-4596(03)00279-2).
- [33] I.M. Hung, W.J. Shih, M.H. Hon, M.C. Wang, The properties of sintered calcium phosphate with  $[\text{Ca}]/[\text{P}] = 1.50$ , Int. J. Mol. Sci. 13 (2012) 13569–13586. <https://doi.org/10.3390/ijms131013569>.
- [34] R.G. Carrodegua, S. De Aza,  $\alpha$ -Tricalcium phosphate: Synthesis, properties and biomedical applications, Acta Biomater. 7 (2011) 3536–3546. <https://doi.org/10.1016/j.actbio.2011.06.019>.
- [35] S. Lala, B. Satpati, S.K. Pradhan, Sintering behavior and growth mechanism of  $\beta$ -TCP in nanocrystalline hydroxyapatite synthesized by mechanical alloying, Ceram. Int. 42 (2016) 13176–13182. <https://doi.org/10.1016/j.ceramint.2016.05.109>.
- [36] M. Frasnelli, V.M. Sglavo, Flash sintering of tricalcium phosphate (TCP) bioceramics, J. Eur. Ceram. Soc. 38 (2018) 279–285. <https://doi.org/10.1016/j.jeurceramsoc.2017.08.004>.
- [37] I.R. Lavagnini, J. V Campos, A.G. Storion, A.O. Lobo, R. Raj, E.M.J.A. Pallone, Influence of flash sintering on phase transformation and conductivity of hydroxyapatite, Ceram. Int. 47 (2021) 9125–9131. <https://doi.org/10.1016/j.ceramint.2020.12.036>.
- [38] B.B. He, Introduction to two-dimensional X-ray diffraction, Powder Diffr. 18 (2003) 71–85. <https://doi.org/10.1154/1.1577355>.
- [39] M.S. Bramble, R.L. Flemming, P.J.A. McCausland, Grain size measurement

- from two-dimensional micro-X-ray diffraction: Laboratory application of a radial integration technique, *Am. Mineral.* 100 (2015) 1899–1911. <https://doi.org/10.2138/am-2015-5181>.
- [40] S.H. Ji, D.S. Kim, M.S. Park, J.S. Yun, Sintering process optimization for 3ysz ceramic 3d-printed objects manufactured by stereolithography, *Nanomaterials.* 11 (2021) 1–12. <https://doi.org/10.3390/nano11010192>.
- [41] C. Shuai, Y. Zhou, Y. Yang, P. Feng, L. Liu, C. He, M. Zhao, S. Yang, C. Gao, P. Wu, Biodegradation Resistance and Bioactivity of Hydroxyapatite Enhanced Mg-Zn Composites via Selective Laser Melting, *Materials (Basel).* 10 (2017) 307. <https://doi.org/10.3390/ma10030307>.
- [42] X.L. Phuah, J. Cho, Akriti, L. Dou, W. Rheinheimer, R.E. García, X. Zhang, H. Wang, Field-assisted growth of one-dimensional ZnO nanostructures with high defect density, *Nanotechnology.* 32 (2021) 95603–95612. <https://doi.org/10.1088/1361-6528/abcb2f>.
- [43] Y. Zhang, J.-I. Jung, J. Luo, Thermal runaway, flash sintering and asymmetrical microstructural development of ZnO and ZnO–Bi<sub>2</sub>O<sub>3</sub> under direct currents, *Acta Mater.* 94 (2015) 87–100. <https://doi.org/10.1016/j.actamat.2015.04.018>.
- [44] B. Yoon, V. Avila, R. Kathiria, L.M. Jesus, Effects of powder dispersion on reactive flash sintering of 8 mol% yttria-stabilized zirconia and MgAl<sub>2</sub>O<sub>4</sub> composites, *Scr. Mater.* 189 (2020) 117–121. <https://doi.org/10.1016/j.scriptamat.2020.08.009>.
- [45] M. Sadat-Shojai, M.T. Khorasani, E. Dinpanah-Khoshdargi, A. Jamshidi, Synthesis methods for nanosized hydroxyapatite with diverse structures, *Acta Biomater.* 9 (2013) 7591–7621. <https://doi.org/10.1016/j.actbio.2013.04.012>.
- [46] N. Méndez-Lozano, R. Velázquez-Castillo, E.M. Rivera-Muñoz, L. Bucio-Galindo, G. Mondragón-Galicia, A. Manzano-Ramírez, M.Á. Ocampo, L.M. Apátiga-Castro, Crystal growth and structural analysis of hydroxyapatite nanofibers synthesized by the hydrothermal microwave-assisted method, *Ceram. Int.* 43 (2017) 451–457. <https://doi.org/10.1016/j.ceramint.2016.09.179>.
- [47] Y.-Z. Wang, Y. Fu, Microwave-hydrothermal synthesis and characterization of hydroxyapatite nanocrystallites, *Mater. Lett.* 65 (2011) 3388–3390. <https://doi.org/10.1016/j.matlet.2011.07.095>.
- [48] W. Rheinheimer, X.L. Phuah, H. Wang, F. Lemke, M.J. Hoffmann, H. Wang, The role of point defects and defect gradients in flash sintering of perovskite oxides,

- Acta Mater. 165 (2019) 398–408.  
<https://doi.org/10.1016/j.actamat.2018.12.007>.
- [49] X.L. Phuah, W. Rheinheimer, Akriti, L. Dou, H. Wang, Formation of liquid phase and nanostructures in flash sintered ZnO, *Scr. Mater.* 195 (2021) 113719.  
<https://doi.org/10.1016/j.scriptamat.2020.113719>.
- [50] S. GRASSO, Y. SAKKA, N. RENDTORFF, C. HU, G. MAIZZA, H. BORODIANSKA, O. VASYLKIV, Modeling of the temperature distribution of flash sintered zirconia, *J. Ceram. Soc. Japan.* 119 (2011) 144–146.  
<https://doi.org/10.2109/jcersj2.119.144>.
- [51] W. Qin, J. Yun, A.M. Thron, K. van Benthem, Temperature gradient and microstructure evolution in AC flash sintering of 3 mol% yttria-stabilized zirconia, *Mater. Manuf. Process.* 32 (2017) 549–556.  
<https://doi.org/10.1080/10426914.2016.1232814>.
- [52] I.R. Lavagnini, J. V. Campos, J.A. Ferreira, E.M.J.A. Pallone, Microstructural evolution of 3YSZ flash-sintered with current ramp control, *J. Am. Ceram. Soc.* 103 (2020) 3493–3499. <https://doi.org/10.1111/jace.17037>.
- [53] J.V. Campos, I.R. Lavagnini, R.V. de Sousa, J.A. Ferreira, E.M. de J.A. Pallone, Development of an instrumented and automated flash sintering setup for enhanced process monitoring and parameter control, *J. Eur. Ceram. Soc.* 39 (2019) 531–538. <https://doi.org/10.1016/j.jeurceramsoc.2018.09.002>.
- [54] R. Chaim, Y. Amouyal, Liquid-film assisted mechanism of reactive flash sintering in oxide systems, *Materials (Basel)*. 12 (2019) 1–9.  
<https://doi.org/10.3390/ma12091494>.
- [55] R. Chaim, Liquid Film Capillary Mechanism for Densification of Ceramic Powders during Flash Sintering, *Materials (Basel)*. 9 (2016) 19–21.  
<https://doi.org/10.3390/ma9040280>.
- [56] J. Janek, C. Korte, Electrochemical blackening of yttria-stabilized zirconia – morphological instability of the moving reaction front, *Solid State Ionics*. 116 (1999) 181–195. [https://doi.org/10.1016/S0167-2738\(98\)00415-9](https://doi.org/10.1016/S0167-2738(98)00415-9).
- [57] M. Biesuz, L. Pinter, T. Saunders, M. Reece, J. Binner, V. Sglavo, S. Grasso, Investigation of Electrochemical, Optical and Thermal Effects during Flash Sintering of 8YSZ, *Materials (Basel)*. 11 (2018) 1214.  
<https://doi.org/10.3390/ma11071214>.
- [58] Y. Dong, I.W. Chen, Electrical and hydrogen reduction enhances kinetics in

- doped zirconia and ceria: II. Mapping electrode polarization and vacancy condensation in YSZ, *J. Am. Ceram. Soc.* 101 (2018) 1058–1073. <https://doi.org/10.1111/jace.15274>.
- [59] L. Wu, C. Zhou, B. Zhang, H. Lei, W. Wang, X. Pu, L. Liu, J. Liang, Y. Fan, X. Zhang, Construction of Biomimetic Natural Wood Hierarchical Porous-Structure Bioceramic with Micro/Nanowhisker Coating to Modulate Cellular Behavior and Osteoinductive Activity, *ACS Appl. Mater. Interfaces.* 12 (2020) 48395–48407. <https://doi.org/10.1021/acsami.0c15205>.